Microstructure by design

Froend, Martin; Ventzke, Volker; Dorn, Falk; Kashaev, N.; Klusemann, Benjamin; Enz, Josephin

Published in:
Materials Science and Engineering A

DOI:
10.1016/j.msea.2019.138635

Publication date:
2020

Document Version
Publisher's PDF, also known as Version of record

Citation for pulished version (APA):
Froend, M., Ventzke, V., Dorn, F., Kashaev, N., Klusemann, B., & Enz, J. (2020). Microstructure by design: An approach of grain refinement and isotropy improvement in multi-layer wire-based laser metal deposition. *Materials Science and Engineering A*, *772*, Article 138635. https://doi.org/10.1016/j.msea.2019.138635

Materials Science & Engineering A 772 (2020) 138635

Contents lists available at ScienceDirect

Materials Science & Engineering A

journal homepage: http://www.elsevier.com/locate/msea

Microstructure by design: An approach of grain refinement and isotropy improvement in multi-layer wire-based laser metal deposition

M. Froend [a,*], V. Ventzke [a], F. Dorn [a], N. Kashaev [a], B. Klusemann [a,b], J. Enz [a]

[a] Helmholtz-Zentrum Geesthacht, Institute of Materials Research, Materials Mechanics, Max-Planck-Straße 1, D–21502, Geesthacht, Germany
[b] Leuphana University of Lüneburg, Institute of Product and Process Innovation, Universitätsallee 1, D-21335, Lüneburg, Germany

ARTICLE INFO

Keywords:
Additive manufacturing
Aluminium alloy
Grain refinement
Laser irradiance
Direct energy deposition
Laser metal deposition

ABSTRACT

The additive production of metallic components with high-throughput is usually associated with high process temperatures and slow cooling rates. This typically results in strongly oriented columnar grain growth along the building direction of the structure having exceedingly large grain sizes. As a result, such structures show typically low strength and anisotropic mechanical behaviour in as-deposited condition. Consequently, post-processing is commonly performed to homogenize and eventually increase the mechanical properties of the deposited structures. In this regard, precise control of the applied process energy allows a modification of the local temperature distribution and cooling conditions during the additive manufacturing process, which strongly influence the resulting solidification microstructure. The aim of the present study is the development of an approach that allows to influence the solidification conditions in wire-based laser metal deposition of an Al-Mg alloy through specific adjustments of the laser irradiation. It was found that significantly different solidification microstructures in as-deposited condition can be achieved by adjusting the laser beam irradiance within a range resulting in conduction mode welding conditions while keeping the heat input constant. The application of high laser beam irradiances, close to the transition to keyhole mode welding, results in structures with a homogeneous large-grained solidification microstructure exhibiting a degree of anisotropy of around 12% between building direction and the direction of deposition. In contrast, the use of low laser beam irradiance close to the lower limit of stable melting, results in structures with a significantly refined microstructure. Consequently, an increase of yield strength of up to around 20% and microhardness of up to 13%, as compared to structures processed with high laser beam irradiance, could be obtained. Moreover, the anisotropy of the as-deposited structure was reduced to a degree lower than 2%.

1. Introduction

Additive manufacturing (AM) in the sense of wire-based direct energy deposition (DED), also referred to as wire-based metal deposition (MD), is a melt-solidification process, in which an energy source such as laser (laser metal deposition, LMD), arc (wire arc additive manufacturing, WAAM), or electron beam (electron beam melting, EBM) is applied to achieve sufficient heat to melt the wire material fed during layer-wise deposition. The mentioned methods stand out for their high potential to realize deposition rates of several kilograms instead of a few hundred grams per hour compared to powder-based AM processes [1–4]. In particular, wire-based LMD and WAAM processes have advantages, such as the sole necessity of a local shielding gas supply to protect the liquefied metal from adverse chemical reactions with atmospheric elements such as oxygen, hydrogen, and nitrogen [5]. In contrast to EBM, which must be performed in an evacuated working chamber, these methods can be integrated into widely used industrial welding systems in a straightforward way [1,4–6]. Regardless the comparably inflexible EBM process, the wire-based MD of Al alloys has mainly been performed by WAAM [6–8]. However, WAAM is mostly associated with high temperatures and limited opportunities to systematically regulate the energy inputs used [9]. This has a significant impact on the evolving microstructures of the deposited structures [7,10]. Since the microstructure formed during the solidification is a key feature that has to be considered regarding the assessment of resulting mechanical properties [11], there has already been significant effort to

---

* Corresponding author. Helmholtz-Zentrum Geesthacht, Institute of Materials Research, Materials Mechanics, Max-Planck-Straße 1, D–21502, Geesthacht, Germany.

E-mail address: martin.froend@hzg.de (M. Froend).

https://doi.org/10.1016/j.msea.2019.138635
Received 25 March 2019; Received in revised form 3 November 2019; Accepted 5 November 2019

reveal and control the grain growth during AM of metal structures [6–8,10,12,13]. In these studies, it was reported that the grain growth in high-throughput deposition processes strongly differs from processes such as SLM. Owing to significantly decreased cooling rates, grain growth during high-throughput MD, such as wire-based LMD, is usually characterized by an inclined growth angle towards the direction of deposition of large columnar grains for unidirectional deposition [14]. Consequently, the resulting microstructure is mostly coarse grained, indicating a strong epitaxial growth in the building direction. It has been reported that typical average grain size is around several hundred microns with a grain aspect ratio of about 0.3 or less [7,8]. In summary, strong anisotropy and poor mechanical properties in as-deposited condition turn out to be a major challenge for wire-based DED, requiring further research [3,7].

Some approaches have been developed to achieve finer microstructures even in the high-throughput MD of non-heat treatable alloys. Zhang et al. [8] reported that the adjustment of suitable inter-layer waiting times up to several minutes, in order to increase the cooling rates during the subsequent layer deposition, has a significant effect on the refinement of microstructures. Furthermore, the authors showed that the control of the pulse rate in WAAM can be used to achieve fine microstructures during the deposition of an Al-Mg alloy [8]. However, the investigated wall-like structures showed an anisotropic tensile mechanical behaviour of $8-27\%$ between building direction and the direction of deposition. At Cranfield University an inter-layer rolling process was developed, which is based on deformation strengthening by means of refining the microstructure mechanically subsequent to deposition, which leads to a reduction of inter-layer porosity as well as an increase of the mechanical properties [15,16]. Gu et al. [7] reported that the application of inter-layer rolling during the WAAM processing of AlMg4.5 results in a significant increase of the microhardness, yield stress (YS), and ultimate tensile strength (UTS) of 140%, 169% and 118%, as compared to the as-deposited condition. However, microstructural characterization revealed that inter-layer rolling supports the development of a strong rolling texture, which is assumed to support the development of anisotropy. Wei et al. [17] also outlined that the heat input in fusion-based metal processing, as a measure of applied heat source power and its velocity along the workpiece, is a strong indicator for the cooling rates during the process. In this regard laser-based processes are known to be precisely adjustable regarding the applied heat inputs [18].

Froend et al. [5,12,19,20] developed an approach for successful wire-based LMD of highly reflective Al-Mg alloy by using an enlarged laser beam diameter. A first analysis of the resulting microstructure revealed certain similarities to the microstructure of WAAM structures. In the work of Froend et al. [19] and Bock et al. [20] the temperature distribution during the developed LMD process was analyzed by thermography and with finite element modeling. The aim of the present study is the use of the obtained knowledge concerning temperature and microstructure evolution during processing of an Al-Mg alloy for tailoring the resulting solidification structure directly during LMD and without any additional process steps, such as inter-layer waiting or rolling. By identifying the laser beam irradiance thresholds for conduction mode and keyhole mode welding, LMD process parameter sets can be derived for obtaining two distinct microstructures. In addition to a detailed microstructural analysis and theoretical considerations on solidification, the impact of the evolving microstructures on the resulting mechanical properties is investigated and discussed.

2. Theoretical considerations

2.1. Development of the solidification microstructure

High process temperatures and low cooling rates support a homogeneous solidification process, resulting in large grains [21]. This is typically expressed by epitaxial grain growth, propagating opposed to the main heat transfer direction, i.e. commonly in building direction in the AM of wall-like structures [22–24]. The morphology of grains can generally be divided into planar, cellular, or dendritic, depending on the solidification condition and the chemical composition of the alloy [22,25]. Based on the considerations of Rosenthal et al. [26], the development of different grain sizes and morphologies in melt-solidification processes is described as a relationship between the temperature gradient G and the growth velocity R during solidification. The product $G \times R$ determines the size of the solidification structure and the G/R ratio determines its morphology in such a way that high values for $G \times R$ yield in fine-grained structures and low values of G/R result in equiaxed-dendritic grains [25,27,28], as it can be seen in Fig. 1 (a).

The microstructure along the height of a single layer deposited is frequently observed to be not homogeneous. It typically consists of epitaxially grown grains near the substrate or the previously deposited layer and more coarse grains near the topside [6,12,23,28]. This is due to the fact that the temperature distribution along the height of one deposited layer is not homogeneous [28]. Following the argumentation of Yan et al. [22], it is stated that the G/R ratio near the bottom of the melt pool typically matches conditions that support the development of columnar-dendritic grain growth. This is predominantly reasoned by the strong heat conduction into the substrate or subjacent structure, thus typically representing the main heat flow direction opposed to the building direction of the structure. Consequently, Al grains typically show a strong alignment with their preferred crystal growth direction to the major local temperature gradient, i.e. the building direction [28]. Less aligned grains are outgrown or suppressed respectively, which is the reason for the denotation of this mechanism as competitive growth mechanism that supports the development of a sharp $\langle 100 \rangle$ texture combined with elongated grain shapes with a major axis orientation along the building direction [12,25].

In contrast, a high G/R ratio typically satisfies the conditions for equiaxed-dendritic grain growth near the topside of a layer [22,28]. Bulk nucleation ahead of the melt pool indicates the transition between the columnar-dendritic grains, growing from the so-called surface epitaxial nucleation to the equiaxed grain morphology near the topside of a layer. This transition is also known as columnar-to-equiaxed transition (CET) [28]. In the CET, the grains can either grow columnar, equiaxed or both growth mechanisms can occur simultaneously [22,25,28]. The described mechanisms are indicated in Fig. 1 (b), in which the typical solidification microstructure for MD along the height of a deposited layer is schematically visualized in accordance with Li et al. [28].

Wang et al. [29] stated that the high-throughput of a comparable cold material in a melt pool can significantly influence the prevailing temperature as well as the flow behaviour of the melt for Ti6Al4V powder-based DED. The cooling effect of the high material feed rate and the resulting generation of turbulences in the melt pool, even during solidification, contributes to an increased distribution of bulk nucleation, whose further growth is constantly interrupted. By this, the CET is shifted into the direction of the subjacent layer, and the majority of the deposited layer solidifies in a refined grain structure with randomized orientation.

2.2. Laser beam irradiance

It has already been shown that process variables, such as the laser power, velocity and rate of deposition, can be used to control the wire-based LMD process [5,6]. Moreover, one important parameter is the laser beam irradiance I. As demonstrated in the literature, it is one of the main parameters for defining the energy input required to melt a material in laser-based fusion processes [30,31]. The laser beam irradiance expresses the applied energy density within a given focal spot area and is given as

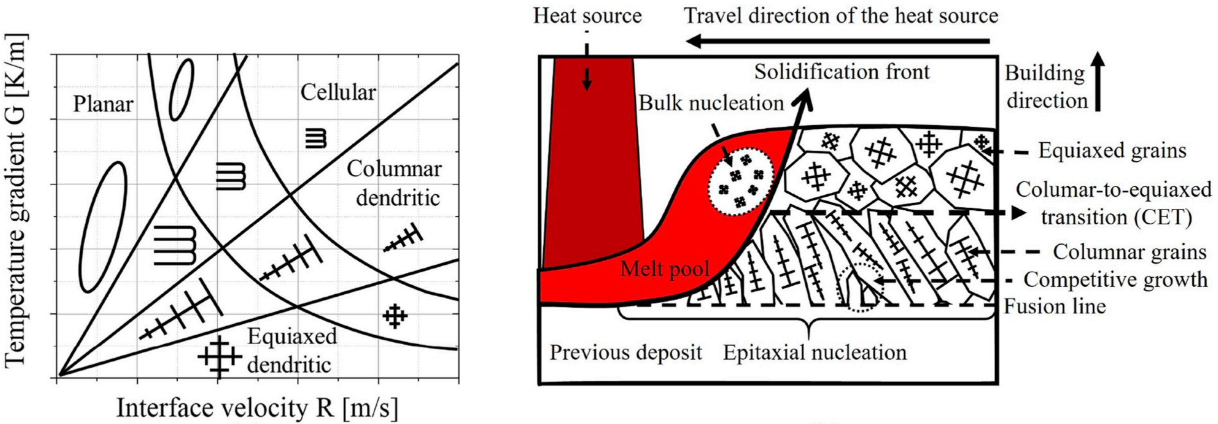

(a) (b)

Fig. 1. (a) The effect of temperature gradient and interface velocity on the grain size and morphology according to Kou et al. [25] and (b) a schematic visualization of possible nucleation and growth mechanisms including their effects on the grain structure evolution in MD according to Li et al. [28].

$$I = \frac{P}{A}. \tag{1}$$

It is dependent on the laser power P and the adjusted focal spot area A. In this regard, A is controlled by adjusting the ratio between the Rayleigh length z_r and the defocusing distance in the transverse direction z relative to the device-specific smallest focal spot diameter d_f taken from [18] as

$$A = \pi\left(\frac{d_z}{2}\right)^2 \tag{2}$$

with the focal spot diameter d_z given as

$$d_z = d_f\sqrt{1 + \left(\frac{z}{z_r}\right)^2}. \tag{3}$$

For laser beam welding (LBW) processes, the device-specific minimum spot diameter is usually adjusted, which is mostly set within a range of several hundred micrometers in order to utilize the maximum efficiency [32–34]. It has also been reported that the adjustment of increased beam diameters can significantly reduce process temperatures, thermal gradients, and the resulting residual stresses [33,35–37]. In wire-based LMD, the adjustment of enlarged focal spot diameters ensures that the entire wire, whose diameter is typically between 0.8 to 1.6 mm, is irradiated, while also some fractions of the substrates surface are captured by the laser spot area. This supports a stable melting and solidification process [20,37]. However, high levels of laser radiation are usually reflected when processing Al. Fig. 2 (a) shows the temperature-dependent absorptivity of pure Al according to Khaskin et al., [38]. It can be seen that the absorption $\mathscr{A}(\lambda, T)$ of pure Al at room temperature is below 3%, but might exceed 16%, when reaching the evaporation temperature. In case of Al-Mg alloys a slightly higher absorptivity is expected. As expressed by Eq. (1), the specific adjustment of increased beam diameters for a constant laser power leads to a reduction of the operating intensity on the target material. Combined with a reduced intensity for large defocusing, the temperature of the irradiated target material increases comparably slow.

The use of high laser intensities on a small spot area results in a very localized increase in the surface temperature of the target material and supports the development of a small melt pool. The absorbed radiation of the laser energy is transmitted through the material by conduction. By this, the temperature of the surrounding material in the vicinity of the beam incidence increases. This again leads to an increase of $\mathscr{A}(\lambda, T)$ and supports the absorption of further supplied heat into the material. It becomes clear that once a melt pool is developed, the efficiency between supplied and absorbed laser energy rapidly increases. The resultant heat accumulation expressed by the melt pool temperature and deep thermal penetration is further supported.

In contrast, a large beam diameter and low laser beam irradiance result in a much less rapid increase of the temperature within the focal spot area. This effect is supported by the development of a reduced laser

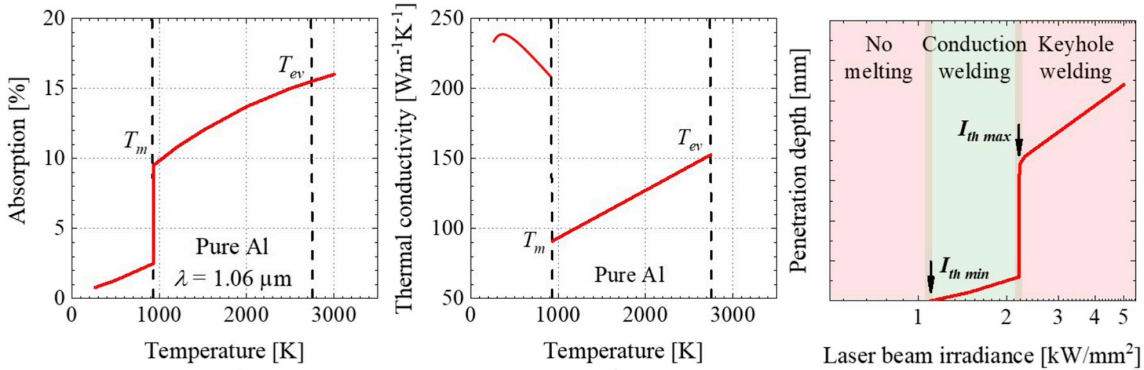

(a) (b) (c)

Fig. 2. (a) Absorptivity of pure Al at different temperatures for a specific wavelength of 1.06 μm [38]. (b) Thermal conductivity of pure Al at different temperatures [41]. (c) Illustration of the calculated threshold laser beam irradiances $I_{th_{min}}$ and $I_{th_{max}}$, see Eqs. (4) and (5), taken as lower and upper boundaries in order to achieve conduction welding conditions (green area), based on the considerations for the LBW of Al-Mg alloys without considering the sample thickness [40]. (For interpretation of the references to colour in this figure legend, the reader is referred to the Web version of this article).

beam irradiance spectrum that reduces the concentration of energy delivered within the beam focus on the surface [18,33]. Critical heat accumulation is reduced as high amounts of energy are reflected.

LBW can be conducted in different modes. Conduction mode or keyhole mode welding. In conduction mode welding, the supplied heat is transferred along the material mainly by heat conduction, which leads to a low thermal penetration and melt pool, respectively. This mode is mostly aspired in AM as the low re-melting depth into subjacent layers also preserves the integrity of the subjacent one. Keyhole mode welding is characterized by the development of a keyhole, in which multiple reflections of the laser irradiation occurs and absorption is significantly higher, as compared to conduction mode welding. Keyhole mode welding during LMD is typically accompanied with high heat inputs, the development of low cooling rates and the development of coarse microstructures in as-deposited condition. Theoretical considerations for the identification of the thresholds in LBW to achieve the melting of a material or to turn into keyhole mode welding were addressed in the past by many pertinent publications, see e.g. [30,31,37,39,40].

The minimum required laser beam irradiance to achieve the melting of a metallic material can be roughly expressed as

$$I_{th_{min}} = \frac{\kappa(T)\,\Delta T}{\mathscr{A}(\lambda,T)\,d_z\,J_{max}}, \tag{4}$$

where $\kappa(T)$ denotes the thermal conductivity, ΔT the temperature difference between the initial temperature of the material T_0 and its melting temperature T_m. J_{max} represents a constant, which is set to 0.52 in case of the application of small beam diameters or low deposition velocities of the heat source [30,31]. In Fig. 2 (b) the temperature dependence of the thermal conductivity is shown according to Mills [41]. It can be seen that thermal conductivity abruptly decreases at the melting temperature and slightly increases with increasing temperature.

The maximum threshold, representing the transition from the conduction mode into the keyhole mode welding, according to Leong et al. [31], is characterized by a deep penetration and a continuous and homogeneous evaporation of the material. For this reason, the evaporation temperature T_{ev} is set as the target temperature, which must be achieved. From this, the maximum laser beam irradiance threshold $I_{th_{max}}$ was derived by Rapp et al. [42] for long dwelling times as

$$I_{th_{max}} = 4\sqrt{\frac{2}{\pi}}\,\frac{\kappa(T)\,T_{ev}}{\mathscr{A}(\lambda,T)\,d_z}. \tag{5}$$

Using these equations, the minimum and maximum thresholds for LBW of Al-Mg alloys were calculated to be around $I_{th_{min}} = 1.1$ kW mm^{-2} and $I_{th_{max}} = 2.2$ kW mm^{-2}.[1] The relationship between the laser beam irradiance and the resulting penetration depth into Al-Mg alloy as well as the identification of $I_{th_{min}}$ and $I_{th_{max}}$ is illustrated in Fig. 2 (c). It can be seen that the penetration depth is the lowest for the lower laser beam irradiance threshold and only marginally increased until the upper laser beam irradiance threshold is reached. This was also experimentally proven by Froend et al. [37].

3. Laser metal deposition process

The wire-based LMD process is shown schematically in Fig. 3. The deposition was carried out in a three-axis, CNC-assisted machining centre with local argon shielding gas supply. The z-axis of the system is equipped with an ytterbium-doped fibre laser having a wavelength of 1.07 μm and maximum power of 8.0 kW. Using a fibre with a diameter of 300 μm and a laser optical system with a focal length of 300 mm resulted in a focal spot diameter 746 μm and a Rayleigh length of 12.3 mm in the LMD experiments. The 1 mm diameter Al-Mg wire (EN AW 5087) was rate-controlled fed onto the Al-Mg substrate material (EN AW 5754) with a thickness of 3 mm in dragging configuration and a feed angle of 35° relative to the substrate surface. During deposition, the platform of the CNC machine was moved relatively to the optical head of the laser system.

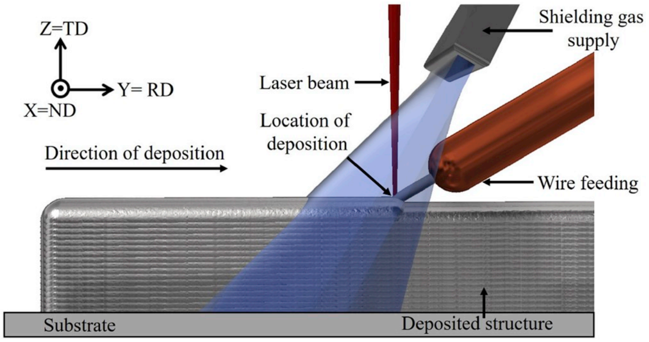

Fig. 3. Schematic visualization of the wire-based LMD process. The laser irradiation is adjusted along the z-axis of the Cartesian coordinate system, representing also the building direction of the structure and the transverse direction (TD) of the substrate. The deposition direction *y* is referred to as RD and the thickness direction *x* of the deposited structure as ND.

Table 1
Process parameters representing the maximum (set 1) and minimum (set 2) laser beam irradiance thresholds.

Fixed process parameters	Symbol	Value	Unit
Laser power	P	4000	W
Deposition velocity	v_t	1	m min^{-1}
Deposition rate	$\dot{m}$	22	g min^{-1}
Deposition length	l	280	mm
Inter-layer waiting time	t	60	s
Argon shielding gas flow rate	Q_{Ar}	10	l min^{-1}
Parameter set 1			
Focal position	z_1	+23	mm
Focal spot area	A_1	2.01	mm^2
Laser beam irradiance	$I_{th_{max}}$	2.2	kW mm^{-2}
Parameter set 2			
Focal position	z_2	+33	mm
Focal spot area	A_2	3.63	mm^2
Laser beam irradiance	$I_{th_{min}}$	1.1	kW mm^{-2}

Based on the considerations given in Section 2, two parameter sets, as summarized in Table 1, are investigated. The parameter sets represent the minimum and maximum laser beam irradiance thresholds for the wire-based LMD process of Al-Mg alloy and have already been shown to result in conduction welding mode as well as in porosity-free structures [37]. The variation of the laser beam irradiance is achieved by a positive defocusing of the optical laser system. Deposition velocity and laser power are kept constant between the parameter sets. Thus, the line energy, also referred to as heat input in AM [6], is equal between both parameter sets.

4. Characterization methods

A fixed specimen geometry of a wall-like structure having a target height and length of 50 mm and 280 mm was defined for deposition. The characterization of the deposited samples was carried out using extractions along the *xz* plane as well as the *yz* plane, which are referred to below as cross and longitudinal sections. They were cut from the middle of the structures at a distance from the start of deposition of 140 mm and a height of 25 mm. Based on these (representative) samples, detailed

---

[1] For calculation of the laser beam irradiance thresholds of the Al-Mg alloy, $T_0 = 25^{\circ}$C, $T_m = 574^{\circ}$C, $T_{ev} = 2100^{\circ}$C, $\mathscr{A}(1.07\,\mu m,\ T_m) = 10\%$, $\mathscr{A}(1.07\,\mu m, T_{ev}) = 16\%$, $\kappa(T_m) = 210$ W/mK and $\kappa(T_{ev}) = 111$ W/mK, $d_z = 2.15$ mm and $J_{max} = 0.52$ were taken according to [38,41].

characterizations of the structures were conducted.

Microstructural observations were performed by using inverted optical microscopy (OM) Leica DMI 5000 M with polarized light. Previously, electrolytic etching using the Barker method was conducted. Subsequently, electron back-scatter diffraction (EBSD) measurements to analyse the microstructural features such as the microtexture were carried out. A working distance of 13 mm at a voltage of 30 kV and a sample tilt of 70° resulting in an effective scan field size of 950 μm × 950 μm were used. The orientation calculation was performed on the basis of the generalized spherical harmonic expansion (GSHE) method in which a triclinic sample symmetry was assumed. The samples were prepared by multi-stage grinding using 500, 800, 1200, 2500, and 4000 abrasive SiC paper. Subsequently, a diamond-polishing using a diamond size of 3 μm and a silicon oxide polishing suspension (OP-S) was applied for final preparation.

Tensile tests according to DIN EN ISO 6892-1 [43] were conducted displacement controlled. The displacement velocity was 0.5 mm/min. Flat tensile specimens having a total length of 50 mm, a testing length of 26 mm, and a thickness of 3 mm were extracted at different locations and orientations with respect to the substrate surface in order to assess the anisotropy of the tensile properties. The samples extracted along the deposition direction are referred to as RD, along the building direction as TD, and tensile specimens extracted with a tilting angle of 45° to RD are referred to as RD-TD direction specimens. The samples were cut from the middle region of the wall-like structure in which stable deposition conditions were present during the process.

Hardness measurements in terms of Vickers hardness testing were conducted in conformity to the standard DIN EN ISO 6507-1 [44]. An indentation time of 10 s at an applied load of 0.3 kg was used. The measurements were arranged from the substrate upward to the topside of extracted specimens.

5. Results and discussion

5.1. Macroscopic appearance

In Fig. 4, optical photographs of the deposited wall-like structures are presented. In case of parameter set 1, 32 layers are required to achieve the targeted structure height having an average thickness of 5.2 mm.[2] Clear surface waves/grooves of increasing and varying depths along the length and height of the structure are observable. After a deposition length of around 230 mm, the structure even lost its geometric integrity, from which it is inferred that the process loses stability with increasing deposition length and height. This is explained by the already reported increase of heat accumulation in deposition and building direction during wire-based MD processes [19,20,37,45]. The roughest surface grooves even partially turn into macroscopic cracks, as illustrated in Fig. 4.

For the deposited structure with parameter set 2, 28 layers are required to reach the defined structure height of 50 mm. The resulting thickness of the wall-like structure shows an average value of 4.8 mm, which is 8% less than for parameter set 1. Significant improvements of the surface quality without surface cracks along the structure are reached, see Fig. 4. Merely at the end of the deposition tracks, near the topside of the structure, a slight decrease of the surface quality can be seen. The comparison of the optical appearance between the structures already allows to conclude that the significantly increased process temperatures in case of parameter set 1 due to the higher laser beam irradiance have greatly affected the solidification behaviour of the structure [37].

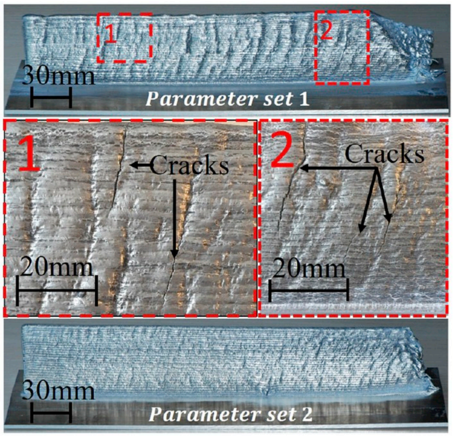

Fig. 4. Photographs of the deposited wall-like structures after wire brush cleaning. The structure produced with parameter set 1 shows strong grooves on the surface, leading partially to macroscopic cracks. After a certain length and height, the process loses stability leading to a lost geometric integrity. Parameter set 2 leads to an improved surface quality of the structure. A reduced number of layers was required to reach the desired height in case of parameter set 2.

In case of parameter set 1, the deposited layers need more time to solidify, which is also expressed by a flatter and wider layer geometry, explaining the increase of the required layers as well as the sample thickness [5]. In case of parameter set 1, a higher fraction of the sample heats up during every additional layer deposition compared to parameter set 2. By this, higher thermal stresses are introduced into the structure, resulting in higher residual stresses [46]. These stresses deform the material expressed by strong surface grooves on the ductile Al. When these stresses exceed the elastic and finally the plastic limit of the material, cracking along the grain boundaries occurs after the melt has solidified, as seen from visual inspection.

5.2. Microstructural characterization

In Fig. 5 (a) and (b), the microstructure evolution along the 15th to the 18th layer processed by parameter set 1 is shown by micrographs obtained from optical microscopy. Both the cross-section and the longitudinal-section show large columnar grains. The major axis orientation is nearly parallel to TD showing a slight tilt towards the direction of deposition. The grains show an average size of several hundred microns and a high aspect ratio resulting in a clear characterization of columnar grains, resulting from a relatively low G/R ratio during the solidification of the deposited material [37]. This leads to the assumption of a strong heat conduction opposed to the building direction. Thus, $\left(\frac{\partial T}{\partial z}\right)$ is stated to be the dominant gradient [37]. The absence of clear transition zones between the layers leads to the conclusion that the energy input of parameter set 1 has indeed resulted in the re-melting of grains deeper than the CET within the subjacent layer, as schematically shown in Fig. 5 (c) and theoretically considered in Section 2. Therefore, the epitaxial microstructure developed a homogeneous progression along the sample height.

According to Herzog et al. [47] and Ho et al. [48], lines of segregations and small microstructure bands can be used for an indication of layer transitions in case of a re-melting depth more than the CET. The achieved average layer height is identified to be 1.5 mm in the present case.[3] In terms of grain orientation, Fig. 6 (a) and (b) show a

---

[2] The thickness or width of the structure is sometimes used interchangeably in the literature. In this work, the wording length, height, and thickness are used to define the geometric dimension of the structure as most common in the literature to LMD.

[3] This value agrees with the calculated height, i.e. 1.56 mm for parameter set 1 and 1.78 mm for parameter set 2.

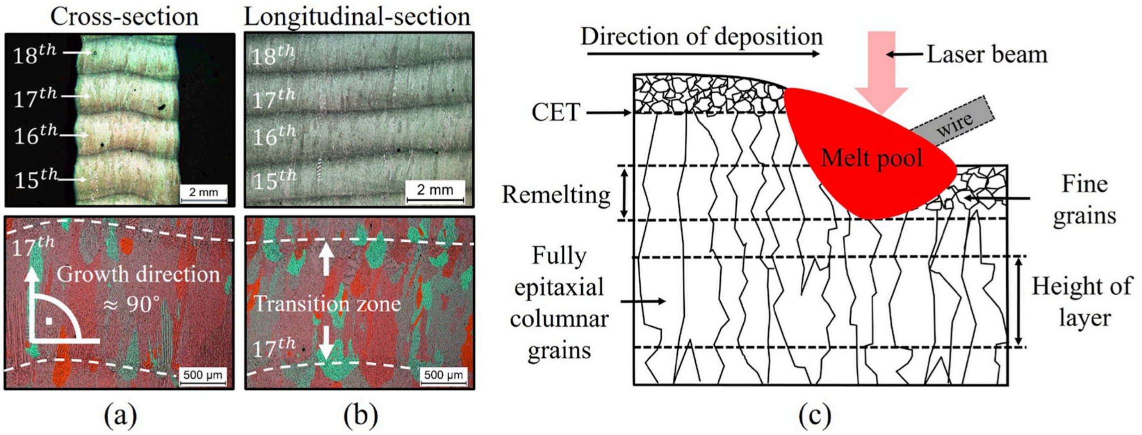

Fig. 5. Cross-section (a) and longitudinal-section (b), capturing the 15th to 18th layer of the wall-like structure processed by parameter set 1 (top), along with an illustration of the optically determined layer transitions and the average height for the 17th layer (bottom) as well as a schematic visualization of the formation of the grain structure during deposition using high laser beam irradiance (c), adapted from [29].

representative orientation map and grain orientation distribution of the 17th layer. The average grain size, according to DIN EN ISO 643 [49], was determined to be 265 μm. Furthermore, grain-boundary angles were determined as plotted in Fig. 6 (c)–(f). In this work, the classification of a single grain is defined by misorientations larger than 5°.

Considering Fig. 6 (d), it can be seen that 91% of the detected grain boundaries are classified as high-angle boundaries, i.e. misorientation larger than 15°. Within single grains, misorientations of less than 5° are detected as well. These are classified as substructures and might be interpreted as distortions of the lattice planes for misorientations lower than 2° [50,51]. Such distortions are assumed to be partial expressions of inherent stresses contributing to the development of dislocations within single grains [50]. The average misorientation angle in terms of the detected substructures and subgrain boundaries within the individual grains was calculated to be 0.56° and most frequently observed within smaller grains within the structure.

It is expected that in case of rapid solidification, these substructures could also develop misorientation angles higher than 5°, thereby leading to the development of new grains and a refined microstructure, respectively [51]. In case of Al, epitaxial grain growth shows a preferential growth orientation along the ⟨001⟩ crystal direction [52]. Considering the calculated (100), (111), and (220) pole figures (PF) from EBSD measurements, plotted in Fig. 7 (a), crystallographic features allowing conclusions regarding the solidification conditions are depicted.

A strong texture sharpness of $H_{max} = 14.62$ mrd along ⟨100⟩ can be seen. This is accompanied by a suggested ⟨100⟩ fibre texture rotating around TD. Furthermore, the ideal texture components {100}⟨001⟩ Cube and {110}⟨001⟩ Goss, which typically are observed in rolled sheet materials, could be identified. These two components strongly indicate a recrystallized microstructure with a strong orientation along the transverse axis of the structure [53]. The observation of these ideal texture components confirms the assumption of the development of high process temperatures combined with slow cooling rates within the structure, as observed for high-throughput wire-based MD processes [6,12,20,37,54].

Regarding the assessment of anisotropy, inverse pole figures (IPF), indicating preferential crystallographic orientations within the deposited structure, are used. In Fig. 7 (b) the IPFs of [001], [100] and [010] representing the preferred crystallographic orientations parallel to ND, RD, and TD are plotted. The ⟨100⟩//[010] crystallographic growth direction shows the maximum intensity. Merely the ⟨101⟩ orientation also occurred parallel to the ND and RD planes as well as the ⟨113⟩ orientation along the RD plane. However, their axial intensities indicate a weak sharpness, which can be neglected compared to the dominant ⟨100⟩ texture along [010]. Texture components as well as their calculated sharpness are summarized in Table 2.

In Fig. 8(a) and (b), representative extractions of the microstructure processed by parameter set 2 capturing the 14th to the 17th layer are shown. The resulting average layer height was measured to be 1.78 mm. The microstructure is characterized by strongly refined grains as well as small regions of epitaxial columnar grains near the layer transitions. In this regard, the grains within the layer (85 μm) are significantly smaller than those in the transition regions (130 μm). The equiaxed and fine microstructure infers a high G/R ratio as well as $G \times R$ relation during deposition, as also observed by Kurz et al. [27], in rapid solidification. The reduced laser beam irradiance, by means of $I_{th_{min}}$, also results in a low re-melting depth into the subjacent structure not exceeding the CET. As a result, the majority of the as-deposited solidification microstructure consists of equiaxed grains. Froend et al. [12,37] have already pointed out that the grain morphology and size of the grains within an underlying deposited layer in wire-based Al-Mg alloy LMD strongly influences the solidification microstructure of the subsequent layer. The authors pointed out that the minor grain axis diameter in the lower part of a deposited layer coincides with the minor axis diameter of the grains within the upper part of the underlying layer. This is also observed for the refined microstructure processed by parameter set 2. The minor grain axis diameters of the equiaxed grain region coincidences with the minor grain axis diameter of the epitaxial grown grains within the lower part of the subsequently deposited layers, as also schematically illustrated in Fig. 8 (c).

Another mechanism that contributes to the development of a refined microstructure is the high feed rate of wire material into the melt. So, the generated melt is assumed to be intermittently unstable, and the occurrence of critical local undercooling supports the generation of heterogeneous nucleation and the development of fine grains respectively.

In Fig. 9 (a) an angular orientation map taken from the extraction of the microstructure along the 16th to the 17th layer is shown. It is divided into two regions. Region I captures the refined grain structure within fractions of the 16th layer, while region II captures the epitaxial transition into the 17th layer.

The angular orientation analysis of the two regions shows significant differences with respect to the major axis of the grains relative to the sample axis. Fig. 9 (b) indicates an almost randomized grain alignment in the fine-grained area. In contrast, Fig. 9 (c) shows a clear preference for the grain orientation toward the transverse direction of the sample within region II. These results indicate that the main part of the structure has a nearly randomized grain orientation, with only a small fraction developing the typical unidirectional solidification structure known

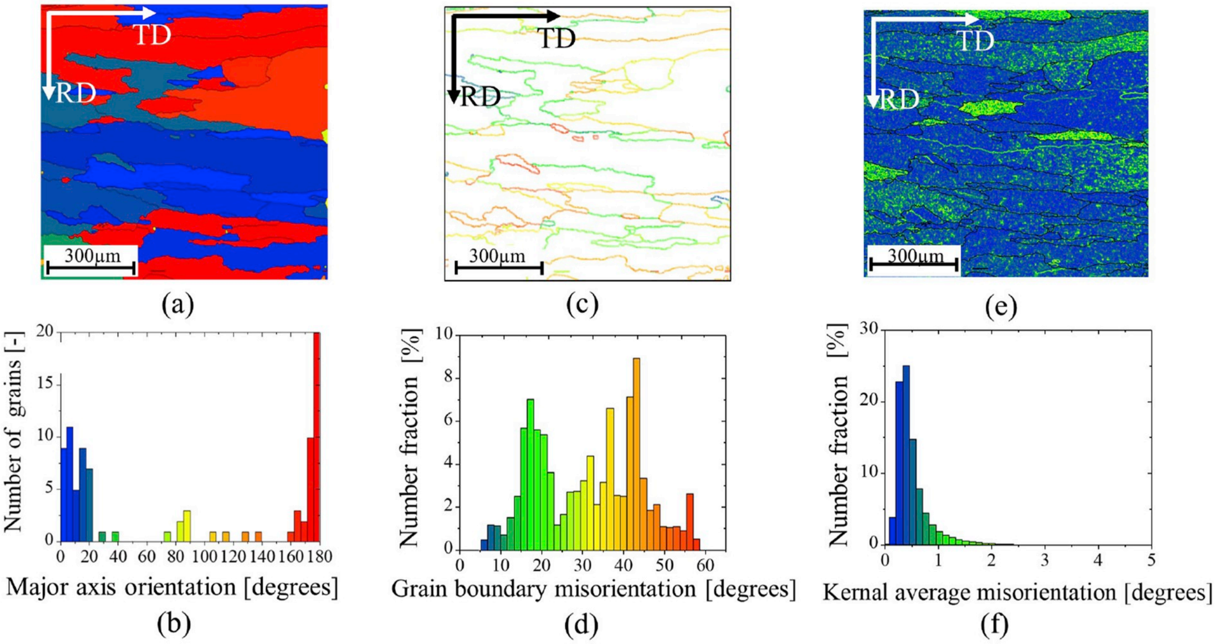

Fig. 6. (a) Angular grain orientation map taken from the 17th layer within the wall-like structure deposited by parameter set 1 as well as (b) the grain orientation angle with respect to the major axis orientation. (c) Grain boundary misorientation map along with (d) the coloured analysis of the detected grain boundary misorientation angles. Additionally, the occurrence of substructures within individual grains, i.e. grains showing misorientation angles lower than 5°, are indicated in (e) and (f).

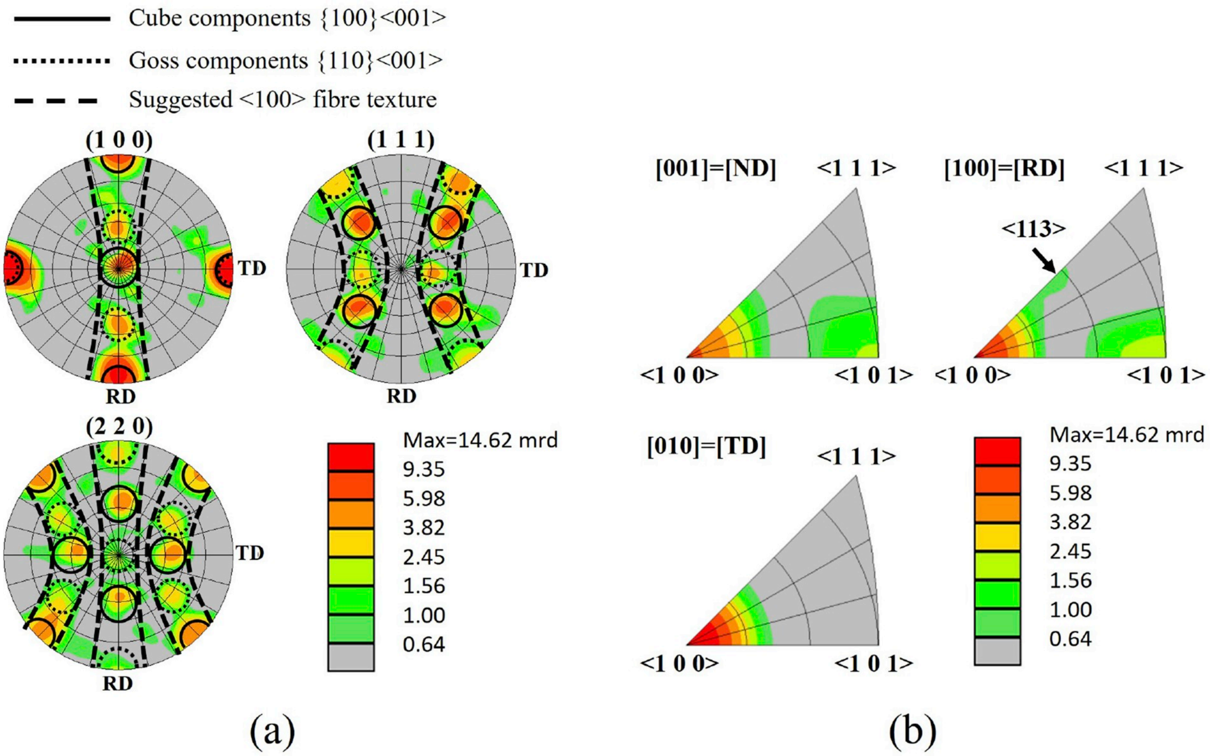

Fig. 7. (a) (100),(111) and (220) pole figures after correction calculations in terms of tilting operations (−8° in RD, −5° in TD and −6° in ND), from which a clear unidirectional solidification supported by an expected ⟨100⟩ fibre as well as ideal texture components such as Cube and Goss within the sample processed with parameter set 1 can be identified. (b) [001], [100] and [010] IPFs, confirm the assumption of sharp ⟨001⟩ solidification texture, as well as show texture components in ⟨101⟩ and ⟨113⟩ directions.

Table 2
Identification and sharpness of the detected crystal orientations within the sample produced using parameter set 1, given in multiple times random [mrd].

Parameter set 1		
$\langle u\,v\,w\rangle//[0\,0\,1]$	$\langle u\,v\,w\rangle//[1\,0\,0]$	$\langle u\,v\,w\rangle//[0\,1\,0]$
$\langle 1\,0\,0\rangle, H = 6.29$	$\langle 1\,0\,0\rangle, H = 9.65$	$\langle 1\,0\,0\rangle, H = 14.62$
$\langle 1\,0\,1\rangle, H = 1.62$	$\langle 1\,0\,1\rangle, H = 1.93$	
	$\langle 1\,1\,3\rangle, H = 0.71$	

from high-throughput MD. Analysis regarding the grain boundary misorientations are presented in Fig. 9 (d)–(g). Interestingly, also high-angle subgrain boundaries were detected, see Fig. 9 (d). Beyond that, misorientations lower than 5° are observed in almost each single grain, which infers a high fraction of subgrain boundaries and dislocations within the microstructure, see Fig. 9 (f) and (g). The observation of substructures within individual grains agrees well with the occurrence of increased cooling rates that could also contribute to residual stresses type two and three [55,56].

Fig. 10 (a) shows the measured crystal orientations within the extracted sample. The (100), (111) and (220) PFs indicate the presence of the {100}⟨001⟩ Cube component as also detected within the structure processed by parameter set 1. However, the observed maximum intensity solely shows a pole density of 3.48 mrd in the (100) PF, i.e. it is around four times weaker than for parameter set 1. Furthermore, the PFs do not show a distinct {110}⟨001⟩ Goss texture component or the development of a ⟨100⟩ fibre texture.

Taking into account the increased amount of measured grains within the sample processed by parameter set 2, which yields an increased grain statistic, this again underlines the development of a less textured and relatively randomized solidification microstructure. This is also supported by the analysis of the [001], [100], and [010] IPFs shown in Fig. 10 (b). Many different crystallographic orientations along all three sample orientations, besides the typical and dominant ⟨100⟩//[010]

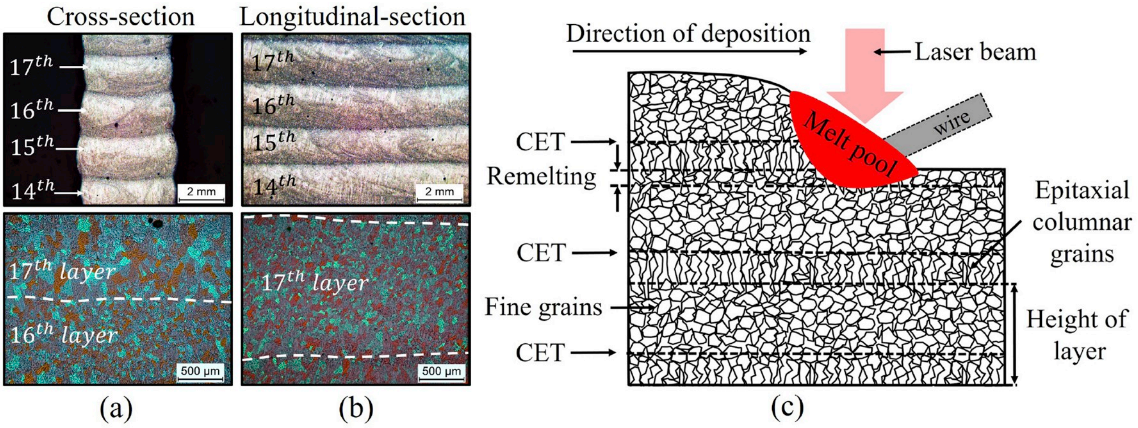

Fig. 8. (a) Cross-section and (b) longitudinal-section capturing the 14^{th} to the 17^{th} layer of the wall-like structure processed by parameter set 2. A refined microstructure comprising mostly equiaxed grains is shown. (c) The schematic visualization of the formation of the grain structure during deposition using $I_{th_{min}}$ adapted from [29] is shown.

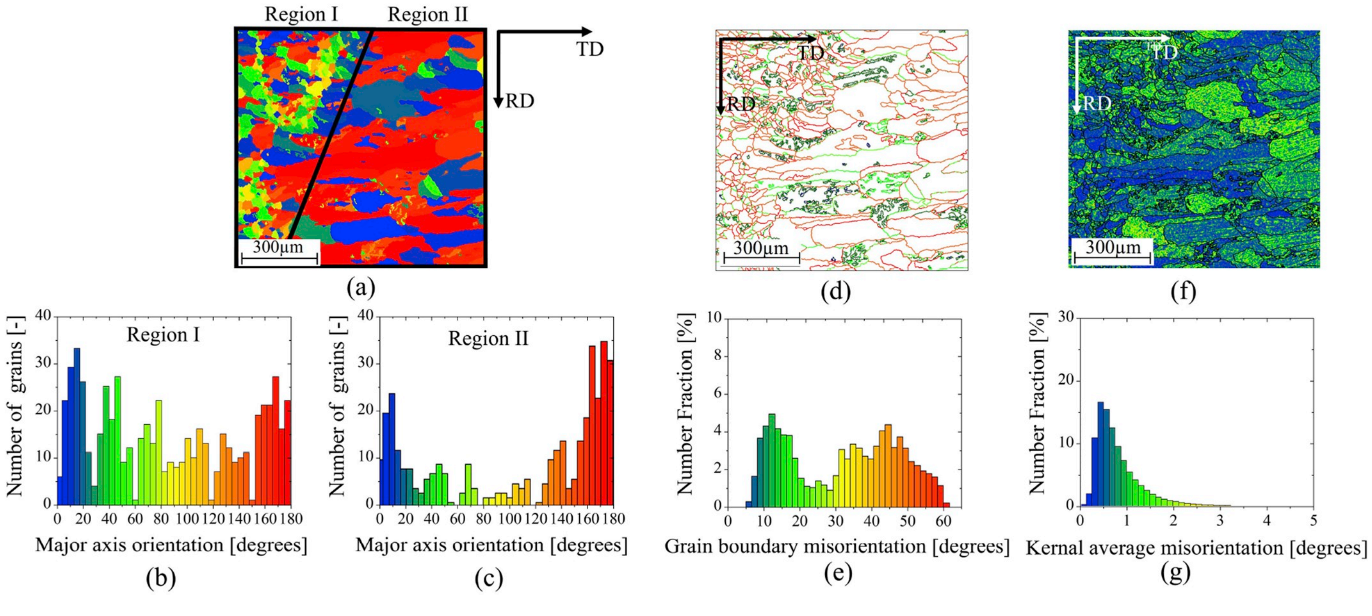

Fig. 9. (a) The angular grain orientation map of a representative extraction within the structure deposited with parameter set 2. An analysis of the angular grain orientation, in which the identified colours correspond to their angular orientation with respect to the substrate surface, is given for (b) the fine-grained region I and (c) the more coarse-grained region II. (d) The grain boundary misorientation map, from which (e) a predominant development of high-angle boundaries compared to the low-angle boundaries is observed. Additionally, the occurrence of substructures within single grains showing misorientations lower than 5° is indicated in (f) as well as classified in (g). (For interpretation of the references to colour in this figure legend, the reader is referred to the Web version of this article).

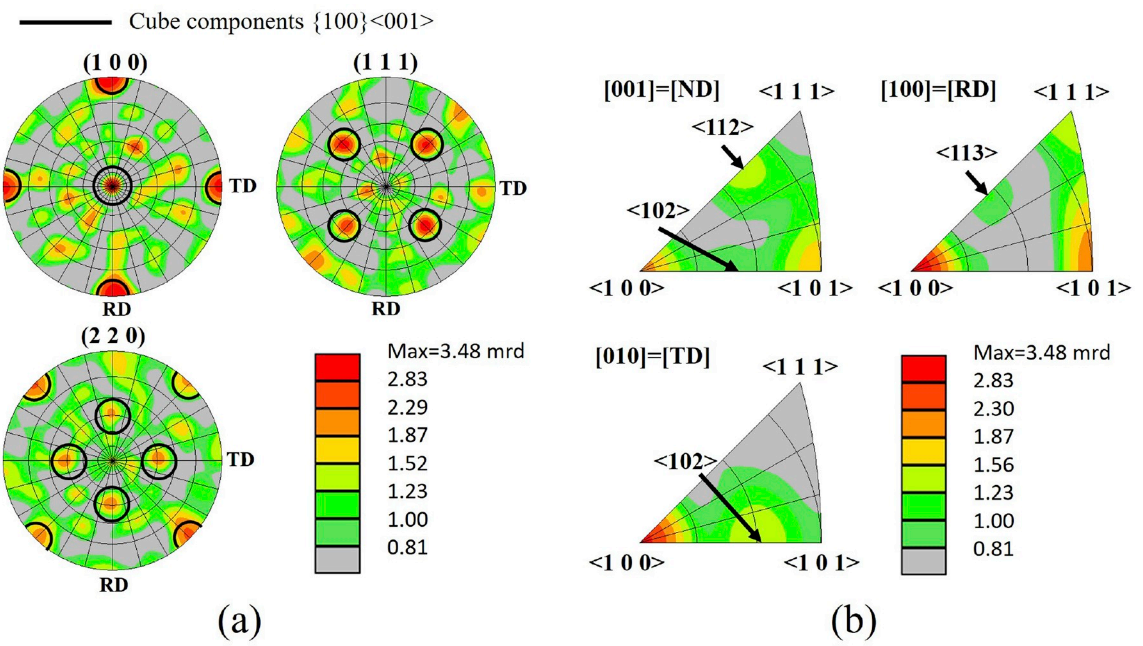

Fig. 10. (a) EBSD measurement results of the sample processed at parameter set 2, showing the (100),(111) and (220) pole figures after correction calculations in terms of tilting operations (+6° in RD, +8° in TD and +5° in ND), from which a decreased texture sharpness and the absence of the Goss as well as fibre texture components are observed. (b) [001], [100] and [010] IPFs show a significantly more randomized texture compared to parameter set 1, combined with the development of several orientation bands along all three sample directions.

orientation, are detected. It is shown that isotropy supporting connection bands along all three sample orientations, such as e.g. from ⟨100⟩ along ⟨102⟩ to ⟨101⟩ parallel to ND and TD or the ⟨101⟩ toward ⟨112⟩ parallel to ND as well as ⟨101⟩ toward ⟨111⟩ parallel to RD, are present. A summary of the detected crystallographic orientations within the sample processed by parameter set 2 is given in Table 3.

The relative orientation of the main slip systems within a polycrystalline material reveals important information regarding the required stresses for initiating crystal slip, i.e. plastic deformation. Considering the results of EBSD measurements, the crystallographic contribution to anisotropy is described by the ratio of Taylor factors calculated for tensile loads along the RD and TD directions of the structures processed with both parameter sets. The Taylor factors, plotted in Fig. 11 (a)–(d), are calculated with respect to the {111}⟨110⟩ glide systems of fcc crystal structures according to Taylor et al. [57].

The distribution and characteristics of the Taylor factors are considerably different for both parameter sets. In case of parameter set 1, the average Taylor factor in TD direction is higher compared to the RD direction, having a ratio RD/TD = 0.89. In contrast, the difference of Taylor factors in case of parameter set 2 is less and their ratio is calculated to be 1.04, representing nearly isotropic conditions. Since the Taylor factors are much lower for the structure produced by parameter set 1, it is expected that the required stress for plastic deformation i.e. the yield strength for the structure processed with parameter set 2 is higher.

Table 3
Identification and sharpness of the crystal orientation within the sample produced by parameter set 2, given in multiple times random [mrd].

Parameter set 2		
$\langle u\,v\,w\rangle//[0\,0\,1]$	$\langle u\,v\,w\rangle//[1\,0\,0]$	$\langle u\,v\,w\rangle//[0\,1\,0]$
$\langle 1\,0\,0\rangle, H = 2.02$	$\langle 1\,0\,0\rangle, H = 3.48$	$\langle 1\,0\,0\rangle, H = 2.99$
$\langle 1\,0\,1\rangle, H = 1.79$	$\langle 1\,0\,1\rangle, H = 2.11$	$\langle 1\,0\,1\rangle, H = 0.88$
$\langle 1\,1\,2\rangle, H = 1.38$	$\langle 1\,1\,1\rangle, H = 1.49$	$\langle 1\,0\,2\rangle, H = 1.51$
$\langle 1\,0\,2\rangle, H = 0.93$	$\langle 1\,1\,3\rangle, H = 1.02$	

5.3. Mechanical characterization

Detailed results of tensile testing are visualized in Fig. 12 for one sample for each tested orientation. A typical jerky flow behaviour of Portevin-Le Châtelier band development expressed by a typical up-down-up stress-strain response over stress-plateau is evident [58]. This behaviour is typically attributed to dynamic strain aging (DSA) in terms of a dynamic interaction between solute elements and mobile dislocations within the matrix [59] and leads to strain-rate-based stress relaxation of the material [58]. Collective unlocking of dislocations expressed by narrow strain localization bands, referred to as PLC bands, occurs. These bands are often subdivided into three types. As can be seen from the tensile test results, hopping bands (type B) characterized by an asymmetric Gaussian-like character, typically observed for intermediate applied strain rates, develop [60].

For parameter set 1, the highest strength was determined in RD, i.e. the deposition direction of the structure. The yield strength was around 12% higher as compared to TD or RD-TD direction, which also represents the degree of tensile yield strength anisotropy. This is explained by the strong columnar grain growth along the building direction of the structure, which yields to a higher amount of grain boundaries within the tensile sample extracted along RD, as compared to TD or RD-TD. Furthermore, a texture strengthening contribution for the yield strength is also assumed. Owing to the strong initial {110}⟨001⟩ Goss texture component, applied tensile loads along RD are oriented around 45° to the {111} family, representing the maximum resolved shear stress. In comparison, the average tensile strength (124 MPa) is around 13% lower as a comparable AlMg4.5 (EN AW 5083) wrought alloy in O-temper condition [7].

In contrast, the structure processed by set 2 shows an increased average yield strength of approximately 142 MPa and significantly reduced anisotropy down to 2%. The yield strength along TD and RD-TD directions is around 16% and 19% higher as compared to that of the structure processed by parameter set 1. This agrees with the Hall-Petch effect, which describes an improvement in the strength and ductility of metallic materials with a refined microstructure [61]. Comparable yield strengths, as reported by Gu et al. [7] (145 MPa) and Horgar et al.

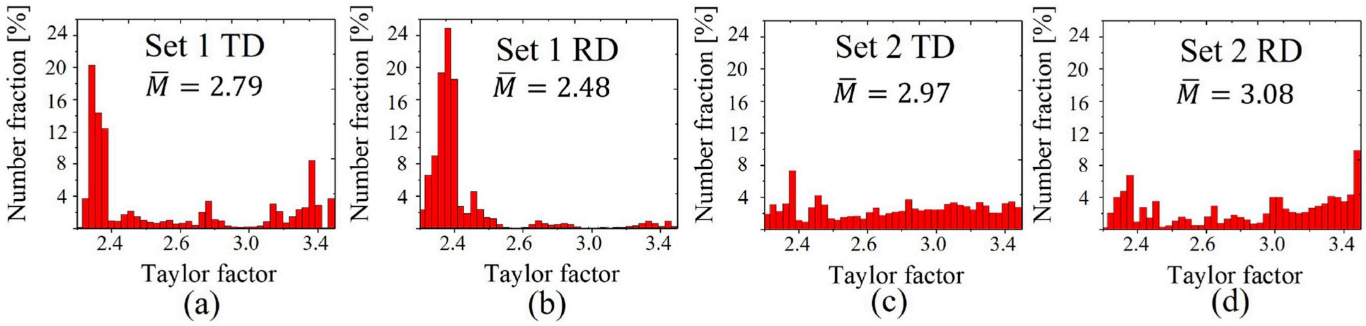

Fig. 11. Calculated Taylor factors M for parameter set 1 (a) in TD and (b) in RD direction as well as for parameter set 2 (c) in TD and (d) in RD direction showing distinct differences between the two parameter sets.

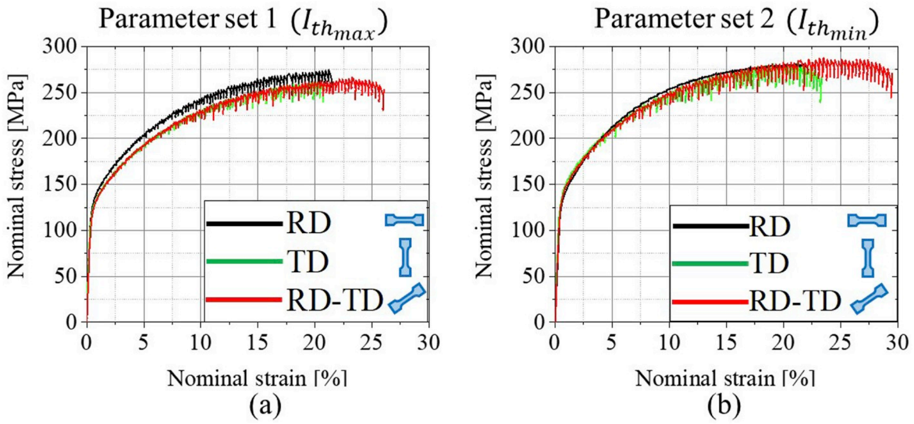

Fig. 12. Results of tensile tests for (a) parameter set 1 and (b) parameter set 2 showing the stress-strain curves for a representative sample for each tested sample orientation. For the structure processed with parameter set 2, an increased level of yield strength and tensile strength, as well as ductility with reduced anisotropy, is observed.

(142 MPa) [7], for WAAM-processed AlMg4.5 alloys in as-deposited condition are achieved. A summary of tensile testing result is given in Table 4.

Following the argumentation of Hansen et al. [61], the resulting yield strength of a metallic material follows an inverse relationship with the average grain size d_{av}, which can be described by means of the Hall-Petch relation as

$$\sigma_{YS} = \sigma_0 + \frac{k_y}{\sqrt{d_{av}}}, \tag{6}$$

where σ_0 and k_y are material-specific constants [61]. σ_0 is a grain-size independent stress, including the contributions from solutes and particles but excluding the contributions of dislocations, and k_y is the strength contribution resulting from the resistance to dislocation motion reasoned in the presence of grain boundaries [61]. The results of calculated yield strength using the experimentally determined average grain sizes and the results from the tensile tests are given in Fig. 13 (a).[4] The slope of the calculated yield strength using Eq. (6) shows excellent agreement to the experimentally determined yield strength. The error bars applied represent the minimum and maximum deviations measured between the three orientations tested, i.e. an expression of the determined anisotropy in the tensile properties.

The detected strengthening increase for the structure processed by parameter set 2 is also confirmed by the results of microhardness testing, see Fig. 13 (b). Constant microhardnesses along the height of the structures of 77 ± 2.3 HV0.3 and 89 ± 1.5 HV0.3 for parameter set 1 and 2 are determined. This corresponds to an increased hardness of around 13% for parameter set 2. For parameter set 1, a slightly increased microhardness is observed for the first layers in close vicinity to the substrate. The microhardness shows a decreasing slope from 85 HV0.3 near the substrate down to around 77 HV0.3 after approximately 10 mm in building direction of the structure. This is explained by the development of finer grains during the deposition of the first layers, as typically increased cooling rates are present in close vicinity to the substrate [12,19,20,37]. The influence of the substrate is not observable for the microhardness determined within the structure processed with parameter set 2. It shows a more constant microhardness along the height of the structure. Comparing the hardness results with those of Gu et al. [7], a comparable microhardness as for WAAM-processed EN AW 5087 wall-like structures using inter-layer rolling at 15 kN is achieved. The significantly decreased average grain size results in a higher level of hardness compared to those measured within the structure processed by

Table 4

Summary of the average tensile mechanical properties determined for the structures processed with parameter set 1 ($I_{th_{max}}$) and parameter set 2 ($I_{th_{min}}$).

Tensile property	Parameter set 1			Parameter set 2			Unit
Testing direction	RD	TD	RD-TD	RD	TD	RD-TD	
Yield strength (YS)	136	120	118	138	143	145	**MPa**
Ultimate Tensile strength (UTS)	275	261	266	280	281	288	**MPa**
Elongation at fracture (A_{frac})	25	21	27	22	23	29	%

---

[4] For the calculation, experimentally determined constants for EN AW 5087 of $\sigma_0 = 102.3$ MPa and $k_y = 384$ MPa $\mu m^{1/2}$ according to Gu et al. [7] were used.

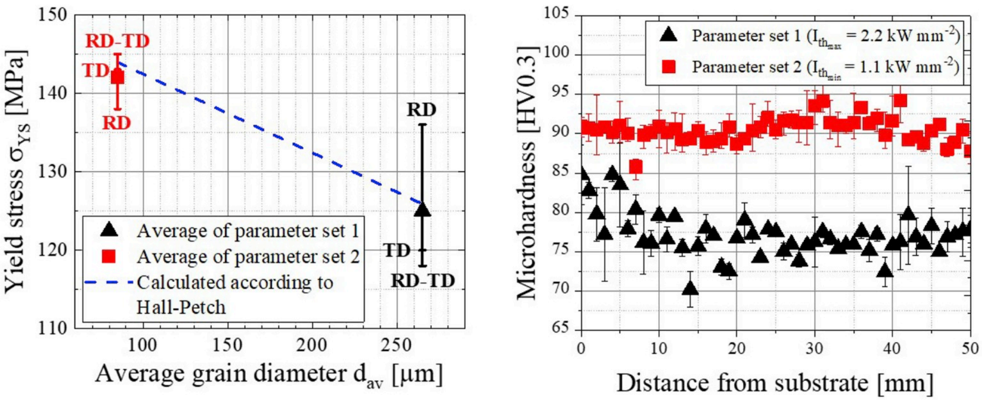

Fig. 13. (a) Tensile test results showing an increased strength for set 2 and a good agreement to the analytical determination using Eq. (6) using the average grain diameters of both parameter sets. The applied error bars represent the minimum and maximum deviations between the three orientations tested. (b) Microhardness measurement results along the height of the wall-like structures processed using parameter set 1 and 2, showing an increased and more homogeneous hardness for set 2.

set 1. Since the chemical composition of the two deposited structures showed no significant differences, the major strengthening contribution is attributed to grain boundary strengthening [37].

The fracture surfaces of tensile specimens processed by parameter set 1 and 2 are given in Fig. 14. In case of parameter set 1, fracture is characterized by a mixture of transcrystalline and shear fracture. An essential feature of transcrystalline fracture is the large number of dimples, as can be seen in Fig. 14 (a) The presence of dimples indicates a ductile fracture mode, which is commonly observed in Al-Mg alloys [7]. As it can also be seen from Fig. 14 (a) fillets at the edges of the formed dimples are observed. These are assumed to be pyramidal flanks or spikes of the {111} glide plane permutations of the fcc crystals. Their detectable surface roughness is attributed to be an indicator of the activation of multiple slip systems during plastic deformation. Additionally, small fractions of shear fracture, as a result of multi-axial stress distributions during plastic deformation, are observed, see Fig. 14 (b). The observation of this fracture characteristic indicates that the present loading conditions are preferentially oriented to active deformation on the {111} glide planes. As a result, smooth intergranular slip was activated and so called shear lips developed.

Representative fracture surfaces of the structures processed with set 2 are shown in Fig. 14 (c) and (d). Generally, high similarities to the fracture surfaces of parameter set 1 are evident. The main fracture mechanism for set 2 is identified on the SEM images to be transcrystalline-normal fracture with fractions of shear fracture. Increased crystallographic randomization, the development of several orientation bands as well as the absence of the {111} ⟨110⟩ Goss and ⟨100⟩ fibre texture components beneficially contribute to the development of multi-axial stress distributions within the refined microstructure. This can also be seen from the magnified fracture surface extractions, in which the development of shear lips having multiple orientations are evident, see Fig. 14 (c) and (d). Based on the analysis of the fracture surfaces for both parameter sets, it can be stated that EN AW 5087 wall-like structures processed by wire-based LMD show a similar

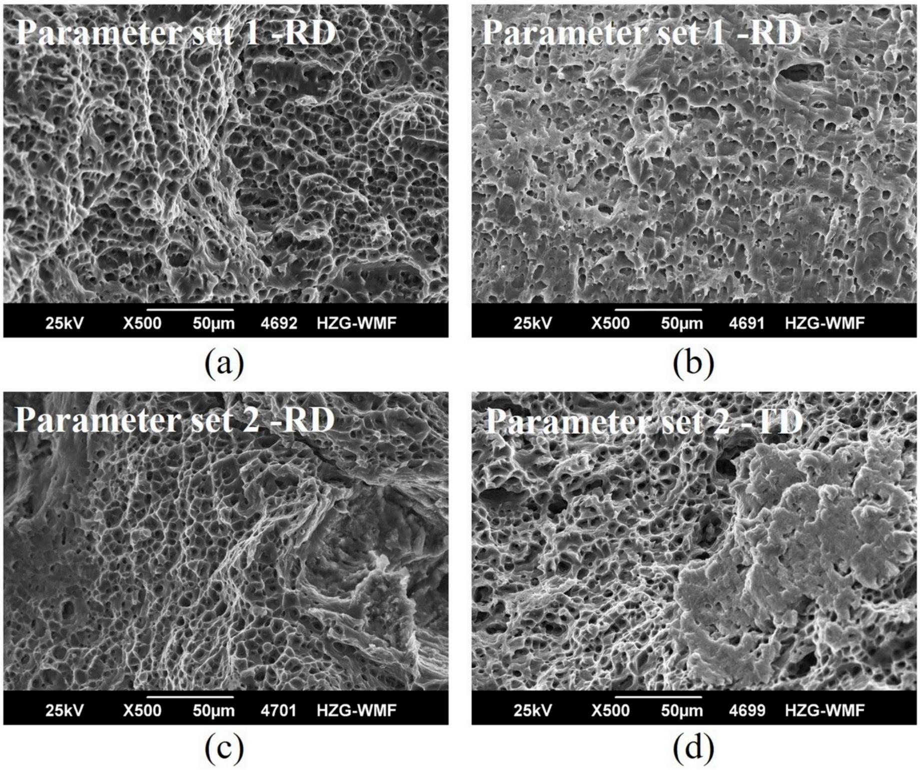

(a) (b)

(c) (d)

Fig. 14. Scanning electron microscopy (SEM) images of the fracture surfaces of tensile specimens processed by (a), (b) parameter set 1 and (c), (d) parameter set 2. Both sets show transcrystalline-normal fracture with fractions of shear fracture.

fracture behaviour as compared to Al-Mg alloys in rolled or cast condition [7].

6. Conclusions

In this research paper, two specific laser beam irradiances were utilized in high-throughput wire-based LMD of an Al-Mg alloy for tailoring the resulting solidification microstructure. The effect on the mechanical properties is studied in depth. Based on the experimental results presented and discussed here, the following conclusions are drawn:

- Specific adjustments of the laser beam irradiance in wire-based LMD of an Al-Mg alloy can significantly affect the resulting solidification microstructure. Thus, laser beam irradiance can be used to achieve distinctly different microstructures and resulting mechanical properties while keeping the heat input constant.
- The considered maximum laser beam irradiance, close to the transition into keyhole mode welding, results in an uniform large-grained epitaxial solidification microstructure leading to anisotropic mechanical behaviour.
- The combination of minimized laser beam irradiance, close to the threshold for melting, and a high-throughput of wire, enables the development of a fine solidification microstructure with nearly isotropic tensile mechanical behaviour.
- Improved tensile properties compared to EN AW 5083 wrought alloy in O-temper condition and similar to WAAM-processed EN AW 5087 can be achieved in the as-deposited condition of the LMD structures.

Declaration of competing interest

The authors declare that they have no known competing financial interests or personal relationships that could have appeared to influence the work reported in this paper.

Acknowledgments

The authors would like to thank Mr. R. Dinse and Mr. P. Haack from Helmholtz-Zentrum Geesthacht for their valuable technical support. B. Klusemann acknowledges support from the Helmholtz-Association via an ERC-Recognition-Award under contract number ERC-RA-0022.

References

[1] A. Ewald, J. Schlattmann, Design guidelines for laser metal deposition of lightweight structures, J. Laser Appl. 30 (3) (2018) 32309.
[2] D. Ding, Z. Pan, D. Cuiuri, H. Li, Wire-feed additive manufacturing of metal components: technologies, developments and future interests, Int. J. Adv. Manuf. Technol. 81 (1) (2015) 465–481, https://doi.org/10.1007/s00170-015-7077-3.
[3] J. Xiong, Y. Lei, H. Chen, G. Zhang, Fabrication of inclined thin-walled parts in multi-layer single-pass GMAW-based additive manufacturing with flat position deposition, J. Mater. Process. Technol. 240 (2017) 397–403, https://doi.org/10.1016/j.jmatprotec.2016.10.019.
[4] M. Schmidt, M. Merklein, D. Bourell, D. Dimitrov, T. Hausotte, K. Wegener, L. Overmeyer, F. Vollertsen, G.N. Levy, Laser based additive manufacturing in industry and academia, CIRP Annals 66 (2) (2017) 561–583, https://doi.org/10.1016/j.cirp.2017.05.011.
[5] M. Froend, S. Riekehr, N. Kashaev, B. Klusemann, J. Enz, Process development for wire-based laser metal deposition of 5087 aluminium alloy by using fibre laser, J. Manuf. Process. 34 (2018) 721–732, https://doi.org/10.1016/j.jmapro.2018.06.033.
[6] T. DebRoy, H. Wei, J. Zuback, T. Mukherjee, J. Elmer, J. Milewski, A. Beese, A. Wilson-Heid, A. De, W. Zhang, Additive manufacturing of metallic components – process, structure and properties, Prog. Mater. Sci. 92 (2018) 112–224, https://doi.org/10.1016/j.pmatsci.2017.10.001.
[7] J. Gu, X. Wang, J. Bai, J. Ding, S. Williams, Y. Zhai, K. Liu, Deformation microstructures and strengthening mechanisms for the wire+arc additively manufactured Al-Mg4.5Mn alloy with inter-layer rolling, Mater. Sci. Eng. A 712 (2018) 292–301, https://doi.org/10.1016/j.msea.2017.11.113.
[8] C. Zhang, Y. Li, M. Gao, X. Zeng, Wire arc additive manufacturing of Al-6Mg alloy using variable polarity cold metal transfer arc as power source, Mater. Sci. Eng. A 711 (2018) 415–423, https://doi.org/10.1016/j.msea.2017.11.084.
[9] B. Wu, Z. Pan, S. van Duin, H. Li, Thermal behavior in wire arc additive manufacturing: characteristics, effects and control, Trans. Intell. Weld. Manuf. (2019) 3–18.
[10] Z. Qi, B. Cong, B. Qi, H. Sun, G. Zhao, J. Ding, "Microstructure and mechanical properties of double-wire+arc additively manufactured Al-Cu-Mg alloys", J. Mater. Process. Technol. 255 (2018) 347–353, https://doi.org/10.1016/j.jmatprotec.2017.12.019.
[11] P. Collins, D. Brice, P. Samimi, I. Ghamarian, H. Fraser, Microstructural control of additively manufactured metallic materials, Annu. Rev. Mater. Res. 46 (1) (2016) 63–91, https://doi.org/10.1146/annurev-matsci-070115-031816.
[12] M. Froend, V. Ventzke, S. Riekehr, N. Kashaev, B. Klusemann, J. Enz, Microstructure and microhardness of wire-based laser metal deposited AA5087 using an Ytterbium fibre laser, Mater. Char. 143 (2018) 59–67, https://doi.org/10.1016/j.matchar.2018.05.022.
[13] C.A. Brice, W.A. Tayon, J.A. Newman, M.V. Kral, C. Bishop, A. Sokolova, Effect of compositional changes on microstructure in additively manufactured aluminum alloy 2139, Mater. Char. 143 (2018) 50–58, https://doi.org/10.1016/j.matchar.2018.04.002.
[14] G. Dinda, A. Dasgupta, J. Mazumder, Texture control during laser deposition of nickel-based superalloy, Scr. Mater. 67 (5) (2012) 503–506, https://doi.org/10.1016/j.scriptamat.2012.06.014.
[15] P.A. Colegrove, J. Donoghue, F. Martina, J. Gu, P. Prangnell, J. Hönnige, Application of bulk deformation methods for microstructural and material property improvement and residual stress and distortion control in additively manufactured components, Scr. Mater. 135 (2017) 111–118, https://doi.org/10.1016/j.scriptamat.2016.10.031.
[16] F. Martina, P.A. Colegrove, S.W. Williams, J. Meyer, Microstructure of interpass rolled wire + arc additive manufacturing Ti-6Al-4V components, Metall. Mater. Trans. A 46 (12) (2015) 6103–6118, https://doi.org/10.1007/s11661-015-3172-1.
[17] H. Wei, H.K.D.H. Bhadeshia, S.A. David, T. DebRoy, Harnessing the scientific synergy of welding and additive manufacturing, Sci. Technol. Weld. Join. 24 (5) (2019) 361–366, https://doi.org/10.1080/13621718.2019.1615189.
[18] E. Beyer, Schweißen mit Laser - Grundlagen, first ed., Springer-Verlag Berlin Heidelberg, 1995, pp. 27–47. Ch. Energieeinkopplung.
[19] M. Froend, F.E. Bock, S. Riekehr, N. Kashaev, B. Klusemann, J. Enz, Experimental investigation of temperature distribution during wire-based laser metal deposition of the Al-Mg alloy 5087, Mater. Sci. Forum (2018) 988–994.
[20] F. Bock, M. Froend, J. Herrnring, J. Enz, N. Kashaev, B. Klusemann, Thermal analysis of laser additive manufacturing of aluminium alloys: experiment and simulation, AIP Conf. Proc. (1960), https://doi.org/10.1063/1.5034996.
[21] H. Wei, J. Mzumder, T. Debroy, Evolution of solidification texture during additive manufacturing, Sci. Rep. 5 (2015), https://doi.org/10.1038/srep16446. No. 16446.
[22] F. Yan, W. Xiong, E.J. Faierson, Grain structure control of additively manufactured metallic materials, Materials 10 (11) (2017), https://doi.org/10.3390/ma10111260.
[23] H. Helmer, A. Bauereiß, R. Singer, C. Körner, Grain structure evolution in Inconel 718 during selective electron beam melting, Mater. Sci. Eng. A 668 (2016) 180–187, https://doi.org/10.1016/j.msea.2016.05.046.
[24] X. Wu, J. Liang, J. Mei, C. Mitchell, P. Goodwin, W. Voice, Microstructures of laser-deposited Ti–6Al–4V, Mater. Des. 25 (2) (2004) 137–144, https://doi.org/10.1016/j.matdes.2003.09.009.
[25] S. Kou, Weld metal solidification II: Microstructure within grains, Welding Metall. 2 (2003) 199–202.
[26] D. Rosenthal, Trans ASME (1946) 849–866.
[27] W. Kurz, B. Giovanola, R. Trivedi, Theory of microstructural development during rapid solidification, Acta Metallurgica 34 (5) (1986) 823–830, https://doi.org/10.1016/0001-6160(86)90056-8.
[28] X. Li, W. Tan, Numerical investigation of effects of nucleation mechanisms on grain structure in metal additive manufacturing, Comput. Mater. Sci. 153 (2018) 159–169, https://doi.org/10.1016/j.commatsci.2018.06.019.
[29] T. Wang, Y. Zhu, S. Zhang, H. Tang, H. Wang, Grain morphology evolution behavior of titanium alloy components during laser melting deposition additive manufacturing, J. Alloy. Comp. 632 (2015) 505–513, https://doi.org/10.1016/j.jallcom.2015.01.256.
[30] K. Leong, H. Geyer, Threshold laser beam irradiances for melting and welding, J. Laser Appl. 9 (5) (1997) 227–231.
[31] K. Leong, H. Geyer, Laser beam welding of any metal, in: Proceedings of the Internaltional Congress on Applications of Laser and Electro-Optics (ICALEO), 1998, pp. 243–251.
[32] J. Enz, M. Kumar, S. Riekehr, V. Ventzke, N. Huber, N. Kashaev, Mechanical properties of laser beam welded similar and dissimilar aluminum alloys, J. Manuf. Process. 29 (2017) 272–280, https://doi.org/10.1016/j.jmapro.2017.07.030.
[33] J. Enz, C. Carrarin, S. Riekehr, V. Ventzke, N. Kashaev, Hot cracking behaviour of an autogenously laser welded Al-Cu-Li alloy, Int. J. Adv. Manuf. Technol. 95 (1) (2018) 299–310, https://doi.org/10.1007/s00170-017-1197-x.
[34] A. Viscusi, C. Leitão, D. Rodrigues, F. Scherillo, A. Squillace, L. Carrino, Laser beam welded joints of dissimilar heat treatable aluminium alloys, J. Mater. Process. Technol. 236 (2016) 48–55, https://doi.org/10.1016/j.jmatprotec.2016.05.006.
[35] M. Windmann, A. Röttger, H. Kügler, W. Theisen, F. Vollertsen, Laser beam welding of aluminum to Al-base coated high-strength steel 22MnB5, J. Mater. Process. Technol. 217 (2015) 88–95, https://doi.org/10.1016/j.jmatprotec.2014.10.026.
[36] S. Meco, L. Cozzolino, S. Ganguly, S. Williams, N. McPherson, Laser welding of steel to aluminium: thermal modelling and joint strength analysis, J. Mater.

Process. Technol. 247 (2017) 121–133, https://doi.org/10.1016/j.jmatprotec.2017.04.002.

[37] M. Froend, V. Ventzke, N. Kashaev, B. Klusemann, J. Enz, Thermal analysis of wire-based direct energy deposition of Al-Mg using different laser irradiances, Addit. Manuf. 29 (2019) 100800, https://doi.org/10.1016/j.addma.2019.100800.

[38] V.Y. Khaskin, V. Korzik, V. Sydorets, A. Bushma, B. Wu, Z. Luo, Improving the efficiency of hybrid welding of aluminum alloys, Pat. Weld. J. 12 (2015) 14–18.

[39] J. Rapp, M. Beck, Fundamental approach to the laser weldability, in: Proceedings of the European Conference of Laser Treatment of Materials (ECLAT), 1994, pp. 313–325.

[40] H. Sakamoto, H. Shibata, F. Dausinger, Laser welding of different aluminium alloys, in: Proceedings of the European Conference of Laser Treatment of Materials (ECLAT), 1992, pp. 125–130.

[41] K.C. Mills, Recommended Values of Thermophysical Properties for Selected Commercial Alloys, Woodhead Publishing, 2002.

[42] J. Rapp, C. Glumann, F. Dausinger, H. Huegel, in: Influence of Processing Parameters and Alloy Composition on the Weld Seam in Laser Welding of Aluminium Alloys, 1992, pp. 99–104.

[43] International Organization for Standardization (ISO 6892–1:2017-02, Metallic materials - tensile testing - Part 1:Method of test at room temperature, Int. Org. Stand. (2017).

[44] International Organization for Standardization (ISO 6507–1:2006, Metallic materials - Vickers hardness test - Part 1: Test, Method, Int. Org. Stand. (2006).

[45] D. Yang, G. Wang, G. Zhang, Thermal analysis for single-pass multi-layer GMAW based additive manufacturing using infrared thermography, J. Mater. Process. Technol. 244 (2017) 215–224, https://doi.org/10.1016/j.jmatprotec.2017.01.024.

[46] J. Zhang, B. Song, Q. Wei, D. Bourell, Y. Shi, A review of selective laser melting of aluminum alloys: processing, microstructure, property and developing trends, Journal of Materials Science and Technology 35(2). https://doi.org/10.1016/j.jmst.2018.09.004, 2019, 270-284.

[47] D. Herzog, V. Seyda, E. Wycisk, C. Emmelmann, Additive manufacturing of metals, Acta Mater. 117 (2016) 371–392, https://doi.org/10.1016/j.actamat.2016.07.019.

[48] A. Ho, H. Zhao, J. W. Fellowes, F. Martina, A. E. Davis, P. B. Prangnell, On the Origin of Microstructural Banding in Ti-6Al4V Wire-Arc Based High Deposition Rate Additive Manufacturing, Acta Mater.doi:https://doi.org/10.1016/j.actamat.2018.12.038.

[49] Internaltional Organization for Standardization, Micrographic determination of the apparent grain size (ISO 643), 2013.

[50] D. Oriwol, E.-R. Carl, A. Danilewsky, L. Sylla, W. Seifert, M. Kittler, H. Leipner, Small-angle subgrain boundaries emanating from dislocation pile-ups in multicrystalline silicon studied with synchrotron white-beam X-ray topography, Acta Mater. 61 (18) (2013) 6903–6910, https://doi.org/10.1016/j.actamat.2013.08.002.

[51] D. Hull, D. Bacon, Introduction to Dislocations, Elsevier Science, 2001, pp. 85–107. Ch. Dislocations in face -centered cubis metals.

[52] J. Hirsch, Textures in industrial processes and products, Mater. Sci. Forum 702 (2012) 18–25.

[53] J. Hirsch, K. Luecke, Mechanism of deformation and development of rolling texture in fcc metal-I description of rolling texture development in homogeneous CuZn alloys, Acta Mater. 36 (1988) 2863.

[54] K. Oyama, S. Diplas, M. M'hamdi, A.E. Gunnæs, A.S. Azar, Heat source management in wire-arc additive manufacturing process for Al-Mg and Al-Si alloys, Addit. Manuf. 26 (2019) 180–192, https://doi.org/10.1016/j.addma.2019.01.007.

[55] R.L. Peng, M. Odén, Y. Wang, S. Johansson, Intergranular strains and plastic deformation of an austenitic stainless steel, Mater. Sci. Eng. A 334 (1) (2002) 215–222, https://doi.org/10.1016/S0921-5093(01)01799-3.

[56] J. Pang, T. Holden, T. Mason, "In situ generation of intergranular strains in an Al7050 alloy", Acta Mater. 46 (5) (1998) 1503–1518, https://doi.org/10.1016/S1359-6454(97)00369-8.

[57] G. Taylor, Plastic strain in metals, 62, J. inst. metals (1938) 307–324.

[58] B. Klusemann, G. Fischer, T. Böhlke, B. Svendsen, Thermomechanical characterization of Portevin–Le Châtelier bands in AlMg3 (AA5754) and modeling based on a modified Estrin–McCormick approach, Int. J. Plast. 67 (2015) 192–216, https://doi.org/10.1016/j.ijplas.2014.10.011.

[59] H. Ait-Amokhtar, C. Fressengeas, S. Boudrahem, The dynamics of Portevin–Le Chatelier bands in an Al–Mg alloy from infrared thermography, Mater. Sci. Eng. A 488 (1) (2008) 540–546, https://doi.org/10.1016/j.msea.2007.11.075.

[60] S. Kok, M. Bharathi, A. Beaudoin, C. Fressengeas, G. Ananthakrishna, L. Kubin, M. Lebyodkin, Spatial coupling in jerky flow using polycrystal plasticity, Acta Mater. 51 (13) (2003) 3651–3662, https://doi.org/10.1016/S1359-6454(03)00114-9.

[61] N. Hansen, Hall–petch relation and boundary strengthening, Scr. Mater. 51 (8) (2004) 801–806, https://doi.org/10.1016/j.scriptamat.2004.06.002.